



Fermi National Accelerator Laboratory

FERMILAB-Pub-93/037-E
E760

Study of the Angular Distribution of the Reaction
 $\bar{p}p \rightarrow \chi_{c2} \rightarrow J/\psi \gamma \rightarrow e^+e^-\gamma$

T.A. Armstrong et al
The E760 Collaboration

*Fermi National Accelerator Laboratory
P.O. Box 500, Batavia, Illinois 60510*

March 1993

Submitted to *Physical Review D*



Disclaimer

This report was prepared as an account of work sponsored by an agency of the United States Government. Neither the United States Government nor any agency thereof, nor any of their employees, makes any warranty, express or implied, or assumes any legal liability or responsibility for the accuracy, completeness, or usefulness of any information, apparatus, product, or process disclosed, or represents that its use would not infringe privately owned rights. Reference herein to any specific commercial product, process, or service by trade name, trademark, manufacturer, or otherwise, does not necessarily constitute or imply its endorsement, recommendation, or favoring by the United States Government or any agency thereof. The views and opinions of authors expressed herein do not necessarily state or reflect those of the United States Government or any agency thereof.

Study of the angular distribution of the reaction

$$\bar{p}p \rightarrow \chi_{c2} \rightarrow J/\psi \gamma \rightarrow e^+e^-\gamma$$

T.A. Armstrong⁶, D. Bettoni², V. Bharadwaj¹, C. Biino⁷, G. Borreani², D. Broemmelsiek⁴,
A. Buzzo³, R. Calabrese², A. Ceccucci⁷, R. Cester⁷, M.D. Church¹, P. Dalpiaz²,
P.F. Dalpiaz², R. Dibenedetto⁷, D. Dimitroyannis⁵, M.G. Fabbri², J.E. Fast⁴, A. Gianoli²,
C.M. Ginsburg⁵, K.E. Gollwitzer⁴, A.A. Hahn¹, M.A. Hasan⁶, S.Y. Hsueh¹, R.A. Lewis⁶,
E. Luppi², M. Macri³, A.M. Majewska⁶, M.A. Mandelkern⁴, F. Marchetto⁷, M. Marinelli³,
J.L. Marques⁵, W. Marsh¹, M. Martini², M. Masuzawa⁵, E. Menichetti⁷, A. Migliori⁷,
R. Mussa⁷, S. Palestini⁷, M. Pallavicini³, N. Pastronc⁷, C. Patrignani³, J. Peoples, Jr.¹,
L. Pesando⁷, F. Petrucci², M.G. Pia³, S. Pordes¹, P.A. Rapidis¹, R.E. Ray^{5,1}, J.D. Reid⁶,
G. Rinaudo⁷, B. Roccuzzo⁷, J.L. Rosen⁵, A. Santroni³, M. Sarmiento⁵, M. Savrié²,
A. Scalisi³, J. Schultz⁴, K.K. Seth⁵, A. Smith⁴, G.A. Smith⁶, M. Sozzi⁶, S. Trokenheim⁵,
M.F. Weber⁴, S.J. Werkema¹, Y. Zhang⁶, J.L. Zhao⁵, G. Zioulas⁴.

(E760 Collaboration)

¹*Fermi National Accelerator Laboratory, Batavia, Illinois 60510, U.S.A.*

²*I.N.F.N. and University of Ferrara, I-44100 Ferrara, Italy*

³*I.N.F.N. and University of Genoa, I-16146 Genoa, Italy*

⁴*University of California at Irvine, California 92717, U.S.A.*

⁵*Northwestern University, Evanston, Illinois 60208, U.S.A.*

⁶*Pennsylvania State University, University Park, Pennsylvania 16802, U.S.A.*

⁷*I.N.F.N. and University of Turin, I-10125 Turin, Italy*

(June 8, 1993)

Abstract

We report on a study of the angular distribution in the reaction $\bar{p}p \rightarrow \chi_{c2} \rightarrow J/\psi \gamma \rightarrow e^+e^-\gamma$. Using a sample of 1904 events, we find that the contribution of helicity zero in the formation process is $B_0^2 < 0.22$ (90% CL), and that the normalized quadrupole amplitude in the radiative decay is $a_2 = -0.14 \pm 0.06$. The normalized radiative decay octupole amplitude, a_3 , is found to be consistent with zero.

13.20.Gd, 13.40.Hq, 14.40.Gx, 13.75.Cs

Typeset using REVTeX

I. INTRODUCTION

In this paper we present the results of an angular distribution analysis for the process

$$\bar{p}p \rightarrow \chi_{c2} \rightarrow J/\psi \gamma \rightarrow e^+ e^- \gamma. \quad (1)$$

The angular distribution is sensitive to the features of the $\bar{p}p$ annihilation process, the properties of the $\bar{c}c$ bound state and the nature of its radiative decay. The data used in this analysis were collected in a high statistics study of charmonium states formed directly in $\bar{p}p$ annihilation at the Fermilab Antiproton Accumulator ring (experiment E760).

Perturbative QCD predicts the helicity zero amplitude in the formation process to vanish, in the limit of massless quarks [1]. Small deviations from these predictions are expected because of non-zero quark masses and non-perturbative effects [2,3].

The angular distribution provides a unique opportunity to study quadrupole and octupole contributions in the radiative decay. The angular distribution is much more sensitive to the presence of higher multipoles than the decay rate. Comparison of measured and predicted values of the quadrupole contribution allows us to test theoretical predictions and to estimate the anomalous magnetic moment of the charmed quark [4,5]. Previous measurements of the quadrupole amplitude [6,7] gave contradictory results. The contribution of the octupole transition provides a test of the single quark radiation hypothesis [8].

II. ANGULAR DISTRIBUTION IN THE HELICITY FORMALISM

The angular distribution of reaction (1) is a function of three angles θ , θ' and ϕ' , which are defined as follows (see also Fig. 1)

θ : the polar angle of the J/ψ with respect to the antiproton, in the center-of-mass system;

θ' : the polar angle of the positron in the J/ψ rest frame with respect to the J/ψ direction in the center of mass system;

ϕ' : the azimuthal angle of the positron in the J/ψ rest frame, where the X' axis is in the plane containing the photon and the antiproton, and $\phi' = 0$ for the antiproton.

Our detector does not distinguish electrons from positrons. However, since charge conjugation invariance requires the angular distribution to be symmetric under the transformation exchanging the two leptons ($\theta' \rightarrow \pi - \theta'$, $\phi' \rightarrow \pi + \phi'$), we can randomly select one of the charged tracks as a positron.

Using the helicity formalism and the above definitions, the angular distribution for reaction (1) can be written as [9,10]

$$W(\theta, \theta', \phi') = \sum_{i=1}^{11} K_i(B_{|\lambda(\bar{p})-\lambda(p)|}, A_{|\lambda(\psi)-\lambda(\gamma)|}) T_i(\theta, \theta', \phi'), \quad (2)$$

where the coefficients K_i depend upon the helicity amplitudes and the T_i 's are functions of the observed angles θ, θ', ϕ' . A full expression for the angular distribution is given in the

Appendix. The helicity amplitudes $B_{|\lambda(\bar{p})-\lambda(p)|}$ and $A_{|\lambda(\psi)-\lambda(\gamma)|}$ parametrize the dynamics of the formation and of the decay processes, respectively. The index $\lambda(\bar{p}) - \lambda(p)$ is equal to the projection of the χ_{c2} spin on the \bar{p} direction, and $\lambda(\psi) - \lambda(\gamma)$ is the projection of the χ_{c2} spin on the J/ψ direction. The amplitudes A_0, A_1, A_2 may be expressed as linear combinations of the multipole transition amplitudes a_1, a_2, a_3 , which are related to the total angular momentum carried by the photon. Since χ_{c2} and J/ψ have opposite parity, the amplitudes a_1, a_2 and a_3 correspond to electric dipole (E1), magnetic quadrupole (M2) and electric octupole (E3) transitions, respectively.

The angular distribution is determined by three independent parameters, obtained from the helicity amplitudes by imposing the two normalization conditions

$$\begin{aligned} B_0^2 + 2B_1^2 &= 1 \\ A_0^2 + A_1^2 + A_2^2 &\equiv a_1^2 + a_2^2 + a_3^2 = 1. \end{aligned} \quad (3)$$

Conventionally B_0^2, a_2, a_3 are chosen as the three independent parameters to be determined, a_1 is taken to be positive, and B_0^2 denotes $|B_0|^2$.

III. EXPERIMENTAL LAYOUT

A. The E-760 target and antiproton beam

The experiment is located in a straight section of the Fermilab Antiproton Source complex [11]. Stochastically cooled antiprotons stored in the Accumulator continuously collide with the internal molecular hydrogen jet target [12]. Peak luminosities of $8 \times 10^{30} \text{ cm}^{-2} \text{ s}^{-1}$ are achieved with a beam of 3.5×10^{11} antiprotons. The r.m.s. momentum spread of the beam at the χ_{c2} is $\sigma(p)/p \approx 2 \times 10^{-4}$, which leads to a center-of-mass energy spread of $\sim 270 \text{ keV}$. A detailed description of the experimental technique and the antiproton beam can be found in Ref. [13].

The data used in this analysis were collected with the antiproton beam energy tuned to the χ_{c2} formation energy, and correspond to the total integrated luminosity of 2.6 pb^{-1} .

B. The detector

The detector (Fig. 2) is a non-magnetic spectrometer with cylindrical symmetry about the beam axis. It is optimized for detection of electromagnetic final states while rejecting a very high hadronic background. The central barrel has full azimuthal acceptance and polar acceptance from 12° to 70° , and the forward end-cap extends polar acceptance to 2° . The detector has been fully described in previous publications [13,14], and is discussed briefly here.

The central detector is built in coaxial cylindrical layers. Two sets of scintillator hodoscopes H1 and H2, with 8-fold and 32-fold azimuthal segmentation respectively, are used for charged particle detection. Tracking is provided by several layers of wire chambers [15–17], with combined r.m.s. resolution of $\sigma(\theta_{lab}) = 4 \text{ mrad}$ and $\sigma(\phi_{lab}) = 7 \text{ mrad}$. A threshold Čerenkov counter [18], with 8-fold azimuthal and 2-fold polar segmentation, is used for electron identification and defines the acceptance at the trigger level $15^\circ \leq \theta_{lab} \leq 65^\circ$.

The outermost component of the central detector is an electromagnetic Central Calorimeter (CCAL) [19], which provides energy and direction measurements for electrons and photons, with r.m.s. resolutions of $\sigma(E)/E \approx 6\%/\sqrt{E(\text{GeV})} + 1.4\%$, $\sigma(\theta_{lab}) = 7\text{ mrad}$ and $\sigma(\phi_{lab}) = 11\text{ mrad}$. The calorimeter is built of 1280 lead-glass blocks pointing to the interaction region, and has a 20 fold polar and 64 fold azimuthal segmentation. For triggering purposes the signals from groups of 9 lead glass counters are summed together to form 160 analog signals. These signals are summed again to provide a coarse $\theta_{lab} - \phi_{lab}$ grid of 40 analog signals for the low level trigger. The 160 signals from the first sums are discriminated and read-out with a set of pattern units with a gate of 30 ns (to be compared to the 150 ns ADC gate) to tag on-time showers. Showers that are not on-time are due to pulse tails from earlier events or (to a lesser extent) from later events.

The forward end-cap is instrumented with an 8-element scintillator hodoscope, followed by four planes of straw tubes and a Forward Calorimeter (FCAL) [20] made up of 144 lead-scintillator sandwich towers that are individually read out through wavelength shifter bars. The FCAL has r.m.s. energy resolution $\sigma(E)/E \approx 19\%/\sqrt{E(\text{GeV})}$, and position resolution $\sigma(x) \approx \sigma(y) \approx 3\text{ cm}$, where x, y are cartesian coordinates in a plane perpendicular to the beam direction. Timing information for FCAL energy deposits is provided by a TDC readout of summed signals coming from 6 groups of 24 FCAL modules.

Luminosity is measured by a solid state detector [21], which counts recoil protons scattered elastically at $\theta_{lab} \approx 86.5^\circ$.

IV. TRIGGER AND EVENT SELECTION

A. Trigger requirements

At the fast trigger level the logic is designed to select, with loose constraints, high mass objects decaying to e^+e^- . The essential elements entering the trigger are: logic signals from the Čerenkov cells, the scintillator hodoscopes (H1 and H2), and the matrix of $5 (\theta_{lab}) \times 8 (\phi_{lab})$ analog sums from the lead glass counters [22]. The analog sums from the central calorimeter coarsely define the positions and energies of electromagnetic showers.

The primary trigger requires that a Čerenkov signal be associated with each of two charged tracks originating from the interaction region, as defined by an appropriate coincidence between elements of the H1 and H2 hodoscopes. Independently we require two showers in the central calorimeter separated by more than 90° in azimuth and with energies above thresholds which depend on the polar angle. The number of accompanying charged particles is only limited by the requirement of ≤ 4 hits in each of the two hodoscopes.

Two additional triggers are implemented to reduce the effects of a localized inefficiency introduced by the septum dividing the polar segments of the Čerenkov counter. This inefficiency affects the identification of electrons in the θ_{lab} region between 33 and 39 degrees. The first auxiliary trigger (A1) requires that one of the two charged tracks be tagged as an electron by the Čerenkov, while in the second auxiliary trigger (A2) the Čerenkov requirement is removed altogether. In both cases, to keep the rate to a reasonable level, only events with charged particle multiplicity of 2 (defined by the number of H1 and H2 hits) are accepted, and a coplanarity constraint requiring the two H2 hits to be separated by 16 ± 1

hodoscope elements is also added. In a background free sample of χ_{c2} events, $\sim 86\%$ of the events are selected by the primary trigger, while $\sim 13\%$ and $\sim 1\%$ are recovered by the auxiliary triggers A1 and A2 respectively.

B. Software event selection

Events in which both the e^+ and the e^- have $15^\circ < \theta_{lab} < 60^\circ$ are accepted, thus avoiding inefficiencies introduced by the detector edges. The event selection is done using only the central calorimeter, since it has a uniform response for electrons in that interval, and its spatial resolution is comparable for electrons to that of the tracking detectors [19]. The CCAL provides the position and energy measurements, while the scintillator hodoscopes and the Čerenkov are used only at trigger level. The calorimeters can detect photons in the range $2^\circ \leq \theta_{lab} \leq 70^\circ$. However, because of interactions of forward photons in material in front of the FCAL, and because of the discontinuity between the two calorimeters, we do not require the photon for event selection.

The software event selection is based on a kinematic fit and on the number of on-time showers. The energies and positions of showering particles are determined by analyzing the energy deposits in a 3×3 grid of calorimeter modules surrounding the hits. A 2C fit to the reaction (1) is performed using only the measured energies and directions of the two electrons. (Energy and momentum conservation and the J/ψ mass provide 5 constraints; if the measured energy and direction of the photon are not used in the fit, the effective number of constraints is $5 - 3 = 2$.)

The very low background level allows us to set a low threshold on the kinematic fit probability ($CL > 0.001$) thus reducing any systematic effects from imperfect knowledge of the calorimeter resolution. The final results of the analysis presented here are insensitive to the precise value of the kinematic fit probability threshold. If the position of the photon is calculated to be outside the acceptance of the calorimeters, we demand that the event contain exactly 2 on-time showers. We otherwise require no more than 3 on-time showers. This cut does not introduce a systematic effect since the extra showers produce an uncorrelated source of inefficiency.

In order to avoid angular bias caused by the charged track coplanarity requirement for the auxiliary triggers, we impose the coplanarity cut on all the events including those from the primary trigger. All acceptance cuts are taken into account when performing the maximum likelihood fits.

Finally, we make two cuts in order to exclude the regions where our determination of θ , θ' and ϕ' is poor, and to further reduce the background. The first cut requires that θ_{lab} of the photon be $< 65^\circ$, removing the majority of the events for which the photon is not detected and consequently the resolution in θ' is poor. The second cut is made on the angle between the electron and the photon. By requiring $|\cos \theta'| < 0.95$ we are able to remove events where the CCAL showers for the electron and the photon overlap. This cut also removes most of the remaining background as determined from a study of off resonance data.

For events in which the photon is detected, a 5C fit to the reaction (1) is performed using all three final state particles in order to improve the accuracy of determination of θ , θ' and ϕ' . The r.m.s. resolutions for the 5C (2C) fit are $\sigma(\cos \theta) \approx 0.01$ (0.05), $\sigma(\cos \theta') \approx 0.01$ (0.08),

and $\sigma(\phi') \approx 0.03$ (0.11) *radians*. More details on the event selection and data analysis can be found in Ref. [23].

The final χ_{c2} sample contains 1904 events. The non-resonant background is estimated by applying the same selection criteria to the event sample collected away from the χ_{c2} resonance, and is found to be 20 ± 3 events, normalized to the same integrated luminosity. Since the event selection is based mainly on the e^+e^- pair, we examine the possibility of a resonant background coming from hadronic transitions of χ_{c2} to J/ψ . This is found to be negligible.

V. ANALYSIS OF THE ANGULAR DISTRIBUTION

A. The maximum likelihood method

The maximum likelihood method is used to find the most probable values of the angular distribution parameters B_0^2 , a_2 and a_3 . The likelihood function is defined as

$$\mathcal{L}(B_0^2, a_2, a_3) = \prod_{j=1}^{N_{events}} P_j(B_0^2, a_2, a_3; \Omega_j), \quad (4)$$

where Ω_j stands for $(\cos \theta_j, \cos \theta'_j, \phi'_j)$. The probability density P_j at Ω_j is a function of the parameters, and is given by

$$P_j(B_0^2, a_2, a_3; \Omega_j) = \frac{W(B_0^2, a_2, a_3; \Omega_j) \alpha(\Omega_j)}{\int W(B_0^2, a_2, a_3; \Omega) \alpha(\Omega) d\Omega}. \quad (5)$$

Here W is the theoretical distribution function (Eq. (2)), $\alpha(\Omega)$ is a product of geometric acceptance and trigger efficiency, and the integral in the denominator is performed over the entire space. The most likely values of the angular distribution parameters B_0^2 , a_2 and a_3 are found by maximizing the likelihood function \mathcal{L} .

The difficulty of performing a 3-dimensional integral for each point in the (B_0^2, a_2, a_3) space in order to maximize the likelihood function can be overcome if we recall that W can be factorized into angle-dependent and amplitude-dependent terms (see Eq. (2)). Using this property, the denominator of Eq. (5) can be written as

$$\int W(B_0^2, a_2, a_3; \Omega) \alpha(\Omega) d\Omega = \sum_{i=1}^{11} K_i(B_0^2, a_2, a_3) F_i, \quad (6)$$

where the constants $F_i = \int T_i(\Omega) \alpha(\Omega) d\Omega$ are independent of the angular distribution parameters, and can be calculated for any acceptance and efficiency configuration using a Monte Carlo integration method.

The fitting procedure was tested on Monte Carlo simulated data. Events were generated according to the theoretical distribution function and then selected using the same cuts as for the data. The results of the maximum likelihood fit on these events agreed within errors with the values assumed in the event generator.

B. Correction for trigger inefficiency

Event detection and reconstruction efficiency is uniform over the fiducial volume; the only potential source of angular bias is trigger inefficiency. The trigger was a logical OR of the primary trigger and two auxiliary triggers, described in section IV A. The goal of combining the triggers was to minimize trigger inefficiency in the region of the Čerenkov partition. However, since the auxiliary triggers had lower efficiency than the primary trigger due to additional requirements on charged particle multiplicity and coplanarity, the combined event sample still suffered from a residual inefficiency in the Čerenkov partition region.

The angular bias due to the coplanarity requirement is removed by imposing this requirement on all events, and accounting for this cut in the definition of geometric acceptance in the likelihood function. This results in a reduction of the total event sample by only 8%. The requirement for multiplicity in the hodoscopes H1 and H2 is the remaining source of inefficiency. The extra hits in the hodoscopes have three sources: δ rays due to interaction of the beam with the target, conversion of the photon in the beam pipe or in the inner tracking detectors, and δ rays due to the interaction of electrons in the tracking detectors.

Two alternative methods are used to correct the data for this inefficiency. In the first method, efficiency of the combined trigger as a function of θ_{lab} is obtained from a study of events

$$\bar{p}p \rightarrow J/\psi \rightarrow e^+e^-, \quad (7)$$

taking into account different kinematics in reactions (1) and (7). This efficiency is then used to get the acceptance \times efficiency function $\alpha(\Omega)$ which appears in Eq. (5).

In the second method the relative efficiency of the auxiliary triggers is obtained by studying a sample of events from reaction (1). The efficiency ϵ , equal to the fraction of events from primary trigger which also satisfy the hodoscope multiplicity requirement, is found to be $\epsilon = (73 \pm 1)\%$, and does not depend significantly on event topology. Events from auxiliary triggers are assigned higher weight in the likelihood function, which is redefined as [24]

$$\mathcal{L}'(B_0^2, a_2, a_3) = \prod_{j=1}^{N_{events}} P_j(B_0^2, a_2, a_3; \Omega_j)^{w_j}. \quad (8)$$

For events coming from primary trigger $w_j = 1$, and for those from auxiliary triggers $w = 1/\epsilon$; the function $\alpha(\Omega)$ of Eq. (5) accounts only for geometric acceptance in this case. This method of treating events with weights can lead to underestimate of statistical errors; however, in our case the effect was found to be negligible.

The two methods give compatible results, which confirms our understanding of trigger inefficiency. It should be noted that the size of the trigger inefficiency correction to the values of the angular distribution parameters is small in comparison with statistical errors.

VI. RESULTS

The results of the likelihood fits are shown in Table I. The statistical errors are determined from the contour on which the likelihood function has decreased by the factor $\exp(-\frac{1}{2})$, corresponding to one standard deviation.

Since the octupole amplitude a_3 is expected to be very small, in the first fit a_3 is assumed to be equal to zero. In the second fit all three parameters are allowed to vary. The octupole amplitude a_3 is found to be consistent with zero, and the values of a_2 and B_0^2 do not change when a_3 is allowed to vary.

The contour plots of the likelihood function in the a_2 - B_0^2 plane with a_3 fixed at zero, and in the a_2 - a_3 plane with $B_0^2 = 0.05$, are shown in Fig. 3. The maximum is well defined in both projections.

The results for B_0^2 can also be interpreted in terms of upper limits. Taking into account the fact that B_0^2 must be non-negative, the corresponding upper limit (90% CL) values are 0.22 for fit 1 and 0.26 for fit 2.

Since the value of the likelihood function does not provide a measure of the goodness of fit, we estimate it using the Pearson's χ^2 test. The data is divided into $5 \times 5 \times 5 = 125$ bins in $\cos \theta$, $\cos \theta'$ and ϕ' , and the χ^2 is calculated using

$$\chi^2 = \sum_{i=1}^{125} \frac{(n_i^{obs} - n_i^{pred})^2}{n_i^{pred}}, \quad (9)$$

where n_i^{obs} is the observed number of events in the i -th bin and n_i^{pred} is the number of events predicted by a Monte Carlo assuming the values of a_2 , a_3 and B_0^2 obtained from the likelihood fit. The χ^2 probabilities of the first and the second fits are found to be 0.18 and 0.16 respectively. The bins with no entries are excluded from the calculation of χ^2 , and in the remaining 111 bins there are only 7 bins with a small number of entries (< 5).

Fig. 4 shows comparison of the data with the best fit on one-dimensional plots in $\cos \theta$, $\cos \theta'$ and ϕ' . The uncorrected data are shown by the shaded histograms. Points with error bars represent the data corrected for acceptance and trigger efficiency, which can be compared directly to the theoretical distribution function. The solid line shows the function $W(\theta, \theta', \phi')$ with parameters a_2 , a_3 and B_0^2 set to the values obtained from the fits.

Our measurement significantly improves the experimental knowledge of the angular distribution parameters. The result for B_0^2 of $0.05_{-0.12}^{+0.11}$ is strong evidence that the contribution of helicity zero in the formation process is small. In the case of a_2 and a_3 , we reduce the statistical errors by approximately a factor of 5 compared to the previous measurements made by the Crystal Ball [6] and R704 [7] collaborations. Our result for a_2 of -0.14 ± 0.06 is in clear disagreement with the value of $0.46 \pm_{0.18}^{0.19}$ obtained by R704; the Crystal Ball result of $-0.33 \pm_{0.29}^{0.12}$ has the same sign as ours but is greater in magnitude.

VII. COMPARISON WITH THEORETICAL PREDICTIONS

A. $\bar{p}p \rightarrow \chi_{c2}$ formation helicity

Helicity conservation in massless perturbative QCD [1] forbids helicity zero in the formation process. However, the basic assumption that the proton consists of massless, collinear quarks is not a good approximation in our case, since the proton mass is of the same order as the χ_{c2} mass. Examples of violations of the QCD helicity selection rule in charmonium are the observations of $\eta_c \rightarrow \bar{p}p$ [25] and $\bar{p}p \rightarrow {}^1P_1$ [26] and a non-zero value of B_0^2 in the decay $J/\psi \rightarrow \bar{p}p$ [27].

The non-zero quark mass can be simply taken into account using the effective lagrangian approach [2], which predicts $B_0^2/B_1^2 = \frac{16}{3}m_p^2/m_\chi^2$ or $B_0^2 = 0.16$. Another prediction comes from a QCD based calculation, which uses the quark-diquark model of the proton [3]. It predicts $B_0^2 = 0.16$ in the scalar diquark limit, and approximately 0.08 in the vector diquark limit. The same model has been used to predict the ratio between the partial widths $\Gamma(\chi_{c1} \rightarrow \bar{p}p)$ and $\Gamma(\chi_{c2} \rightarrow \bar{p}p)$, and the experimental result is consistent with a scalar diquark dominance.

Our result for B_0^2 is compatible with all the above predictions. Within statistical errors, we are not able to distinguish between the massless QCD predictions and the models incorporating non-zero quark mass.

B. Multipolarity of the radiative decay $\chi_{c2} \rightarrow J/\psi \gamma$

The higher multipoles arise naturally in the relativistic description of the interaction between the electromagnetic field and the quarkonium system [28]. The contributions of higher multipoles to the radiative decay rates of charmonium are relatively small, of the order of E_γ^2/m_c^2 for the quadrupole amplitude (where E_γ is the photon energy and m_c is the charmed quark mass). In addition, theoretical predictions for the decay rates have significant uncertainties due to potential dependence, relativistic corrections and coupled channel effects. On the other hand, the contribution of higher multipoles to angular distributions in radiative decays appears to first order in E_γ/m_c .

The quadrupole amplitude a_2 has been calculated in Ref. [4,5] and to the first order in E_γ/m_c (or v^2/c^2) it is independent of the potential. The amplitude is proportional to the magnetic moment of the charmed quark, and can be written as¹

$$a_2 = -\frac{3}{\sqrt{5}} \frac{E_\gamma}{4m_c} (1 + \kappa_c). \quad (10)$$

The anomalous magnetic moment κ_c measures the deviation of the magnetic moment from that of a free Dirac particle. Higher order relativistic corrections to Eq. (10) are potential-dependent, and have not been fully calculated. The relative size of these corrections is of the order $v^2/c^2 \approx 15\%$. A part of these corrections, due to relativistic and retardation effects on the E1 amplitude, can be calculated using the results of Ref. [4] and is approximately 5%.

Since κ_c is expected to be small [4], we first compare our result to the prediction assuming $\kappa_c = 0$ and $m_c = 1.5$ GeV. Our result is in agreement with the predicted value of $a_2 = -0.10$. Alternatively, we can treat our result as a measurement of κ_c , obtaining

$$\kappa_c = 0.46 \pm 0.62 \pm 0.37, \quad (11)$$

where the first error is statistical and the second is due to the uncertainty of m_c (± 0.3 GeV) and the theoretical uncertainties in computing a_2 .

Several other quantities related to charmonium depend on the anomalous magnetic moment κ_c . In the non-relativistic limit the rate of M1 transition $J/\psi \rightarrow \eta_c \gamma$ is proportional to

¹We have corrected a misprint in Eq.41 of Ref. [4].

the square of the magnetic moment of the charmed quark [29]. However, relativistic effects are important in M1 transitions, so one should use relativistic calculations to extract the value of κ_c . Comparing the prediction for the $J/\psi \rightarrow \eta_c \gamma$ width [30] (assuming a scalar confining potential) with the experimental value [25] one obtains $\kappa_c = -0.01 \pm 0.10$, with the error due to experimental uncertainty only. An analogous comparison for the rate of the hindered decay $\psi' \rightarrow \eta_c \gamma$ implies a value of $\kappa_c \approx -1$ in the formalism of Ref. [30]; however, this rate is very model-dependent and other effects such as coupled channels [31] or sensitivity to the potential [32] can explain it without the need of a large anomalous magnetic moment. The E1 transition rates, $\psi' \rightarrow \chi_{cJ} \gamma$ and $\chi_{cJ} \rightarrow J/\psi \gamma$, also receive corrections due to the anomalous magnetic moment [28,30]. These corrections are of the order of only a few percent and it is impossible to extract the value of κ_c with reasonable accuracy.

It is interesting to consider the ratio of the quadrupole amplitudes in radiative decays of χ_{c2} and χ_{c1} . The theoretical uncertainties due to quark mass and anomalous magnetic moment cancel out in the ratio (to the first order in E_γ/m_c), and the predicted value is $a_2(\chi_{c2})/a_2(\chi_{c1}) = \frac{3}{\sqrt{5}} \frac{E_\gamma(\chi_{c2})}{E_\gamma(\chi_{c1})}$ [4]. Using this ratio and our value of $a_2(\chi_{c2})$, we predict that $a_2(\chi_{c1}) = -0.09 \pm 0.04$, which is 2.3 standard deviations away from the value of $0.00 \pm_{0.02}^{0.01}$ measured by the Crystal Ball collaboration [6].

The octupole amplitude a_3 is predicted to vanish by the single quark radiation hypothesis [8]. If the photon is emitted by a single quark, the vanishing of the octupole amplitude is a consequence of angular momentum conservation, provided that J/ψ is in a pure S-wave state. Even if there is an admixture of D-wave in the J/ψ , deviation from $a_3 = 0$ is expected to be negligibly small [4,30]. Our result is consistent with the prediction of the single quark radiation hypothesis.

ACKNOWLEDGEMENTS

The authors wish to acknowledge the support of the Fermilab staff and technicians, and in particular the help of the members of the Accelerator Division. We also wish to thank the staff and technicians at our respective institutions for their help and cooperation.

This research was supported in part by the U.S. Department of Energy, the U.S. National Science Foundation and the Istituto Nazionale di Fisica Nucleare of Italy.

APPENDIX: FULL EXPRESSION FOR THE ANGULAR DISTRIBUTION

The angular distribution for the reaction $\bar{p}p \rightarrow \chi_{c2} \rightarrow J/\psi \gamma \rightarrow e^+e^-\gamma$ can be written as follows

$$W(\theta, \theta', \phi') = \sum_{i=1}^{11} K_i(B_{|\lambda(\bar{p})-\lambda(p)|}, A_{|\lambda(\psi)-\lambda(\gamma)|}) T_i(\theta, \theta', \phi'). \quad (A1)$$

The helicity amplitudes B_0, B_1 , and A_0, A_1, A_2 parametrize the dynamics of the formation and decay processes, respectively; the angles θ, θ' and ϕ' are defined in Sec. II, and the coefficients K_i and the functions T_i are given below.

The amplitudes A_0, A_1, A_2 can be expressed in terms of the multipole transition amplitudes a_1, a_2, a_3 [33]

$$\begin{aligned} A_0 &= \sqrt{\frac{1}{10}}a_1 + \sqrt{\frac{1}{2}}a_2 + \sqrt{\frac{6}{15}}a_3, \\ A_1 &= \sqrt{\frac{3}{10}}a_1 + \sqrt{\frac{1}{6}}a_2 - \sqrt{\frac{8}{15}}a_3, \\ A_2 &= \sqrt{\frac{6}{10}}a_1 - \sqrt{\frac{1}{3}}a_2 + \sqrt{\frac{1}{15}}a_3. \end{aligned} \tag{A2}$$

The following normalization conditions are imposed on the helicity amplitudes

$$\begin{aligned} B_0^2 + 2B_1^2 &= 1 \\ A_0^2 + A_1^2 + A_2^2 &\equiv a_1^2 + a_2^2 + a_3^2 = 1. \end{aligned} \tag{A3}$$

Table II gives full expressions for the coefficients K_i and the functions T_i that appear in Eq. (A1); they were taken from Ref. [9]. The constant R is defined as

$$R \equiv \frac{2B_1^2}{B_0^2 + 2B_1^2} = 2B_1^2. \tag{A4}$$

REFERENCES

- [1] S. J. Brodsky, G. P. Lepage, Phys. Rev. D **24**, 2848 (1981); A. Andrikopoulou, Z. Phys. C **22**, 63 (1984).
- [2] W. Buchmüller, preprint CERN-TH.4142/85, (Proc. III LEAR Workshop - Tignes 1985), 327; the result for B_0^2/B_1^2 given in Sec. VII A comes from our calculation, and is larger than the value quoted in this reference by a factor of ~ 2 .
- [3] M. Anselmino *et al.*, Phys. Rev. D **45**, 4340 (1992); **44**, 1438 (1991); **38**, 3516 (1988).
- [4] K. J. Sebastian, H. Grotch, F. L. Ridener, Jr., Phys. Rev. D **45**, 3163 (1992).
- [5] G. Karl, S. Meshkov and J. L. Rosner, Phys. Lett. **45**, 215 (1980).
- [6] M. Oreglia *et al.*, Phys. Rev. D **25**, 2259 (1982).
- [7] C. Baglin *et al.*, Phys. Lett. B **195**, 85 (1987).
- [8] M. G. Olsson *et al.*, Phys. Rev. D **31**, 1759 (1985), and references therein.
- [9] F. L. Ridener, Jr., K. J. Sebastian, H. Grotch, Phys. Rev. D **45**, 3173 (1992).
- [10] M. G. Olsson *et al.*, Phys. Rev. D **34**, 2043 (1986); A. D. Martin *et al.*, Phys. Lett. **147B**, 203 (1984).
- [11] J. Peoples Jr., Prospects for $\bar{p}p$ experiments in the TeV I accumulator, in Low energy antimatter, Proc. Workshop on the design of a low energy antimatter facility, October 1985, ed. D. Cline (World Scientific, Singapore, 1986).
- [12] M. Macrí, Gas jet targets, CERN Accelerator School 1983, CERN 85-15 (1985).
- [13] T. A. Armstrong *et al.*, Phys. Rev. D **47**, 772 (1993).
- [14] T. A. Armstrong *et al.*, Nucl. Phys. B **373**, 35 (1992).
- [15] C. Biino *et al.*, Nucl. Instrum. & Methods. A **271**, 417 (1988); IEEE Trans. Nucl. Sci. **36**, 98 (1989).
- [16] R. Calabrese *et al.*, Nucl. Instrum. & Methods A **277**, 116 (1989); IEEE Trans. Nucl. Sci. **36**, 54 (1989).
- [17] G. Barisone *et al.*, Report No. INFN-Genoa/AE-89/6, 1989 (unpublished).
- [18] C. Biino *et al.*, Nucl. Instrum. & Methods A **317**, 135 (1992).
- [19] L. Bartoszek *et al.*, Nucl. Instrum. & Methods A **301**, 47 (1991).
- [20] M. A. Hasan *et al.*, Nucl. Instrum. & Methods A **295**, 73 (1990).
- [21] M. Sarmiento *et al.*, A luminosity monitor for FNAL experiment E-760, to be submitted to Nucl. Instrum. & Methods.
- [22] R. Ray *et al.*, Nucl. Instr. & Methods A **307**, 254 (1991).
- [23] R. Mussa, Ph.D. thesis, University of Turin, Italy, 1992 (unpublished); A. M. Majewska, Ph.D. thesis, Pennsylvania State University, 1992 (unpublished); J. L. Marques, Ph.D. thesis, University of California, Irvine, 1992 (unpublished).
- [24] A. G. Frodesen, O. Skjeggstad and H. Tøfte, *Probability and Statistics in Particle Physics*, Universitetsforlaget, Bergen-Olso-Tromsø (1979).
- [25] Particle Data Group, K. Hikasa *et al.*, Phys. Rev. D **45**, S1 (1992); **46**, 5210(E) (1992).
- [26] T. A. Armstrong *et al.*, Phys. Rev. Lett. **69**, 2337 (1992).
- [27] D. Pallin *et al.*, Nucl. Phys. B **292**, 653 (1987).
- [28] R. McClary, N. Byers, Phys. Rev. D **28**, 1692 (1983);
M. A. Doncheski, H. Grotch, K. J. Sebastian, Phys. Rev. D **42**, 2293 (1990).
- [29] W. Kwong, J. L. Rosner and C. Quigg, Ann. Rev. Nucl. Part. Sci. **37**, 325 (1987).
- [30] H. Grotch, D. A. Owen, K. J. Sebastian, Phys. Rev. D **30**, 1924 (1984).
- [31] V. Zambetakis and N. Byers, Phys. Rev. D **28**, 2908 (1983).

- [32] X. Zhang, K. J. Sebastian, H. Grotch, Phys. Rev. D **44**, 1606 (1992).
- [33] G. Karl, S. Meshkov and J. L. Rosner, Phys. Rev. D **13**, 1203 (1976).

FIGURES

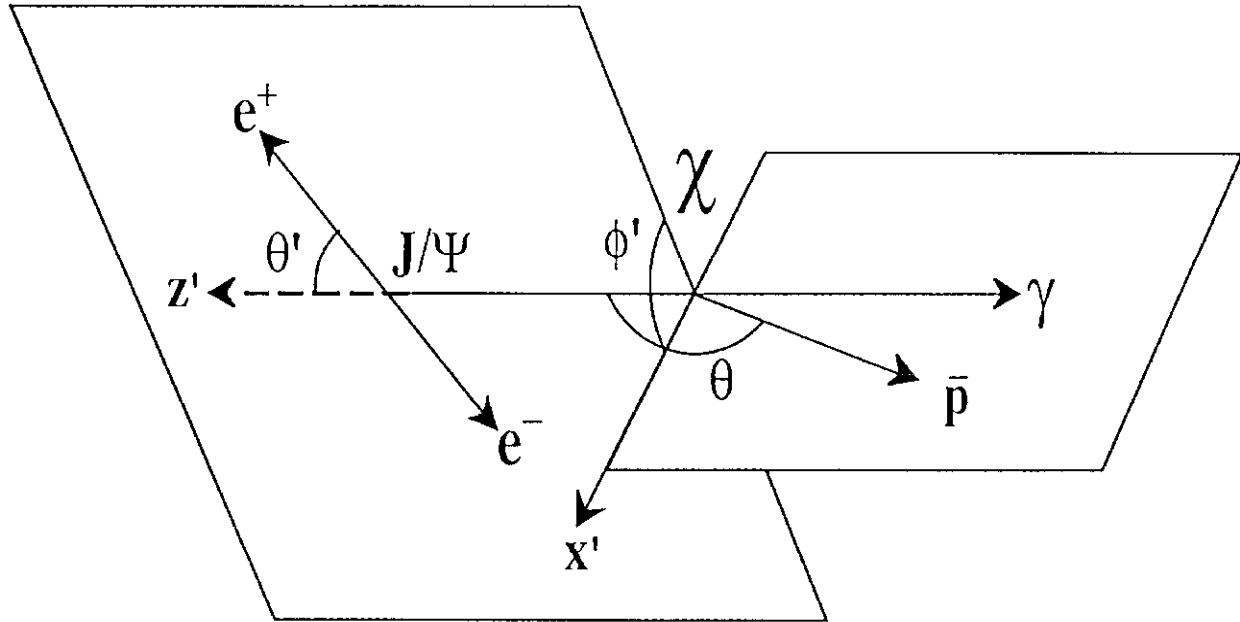


FIG. 1. Definition of the angles: θ in the χ_{c2} rest frame, and θ' , ϕ' in the J/ψ rest frame.

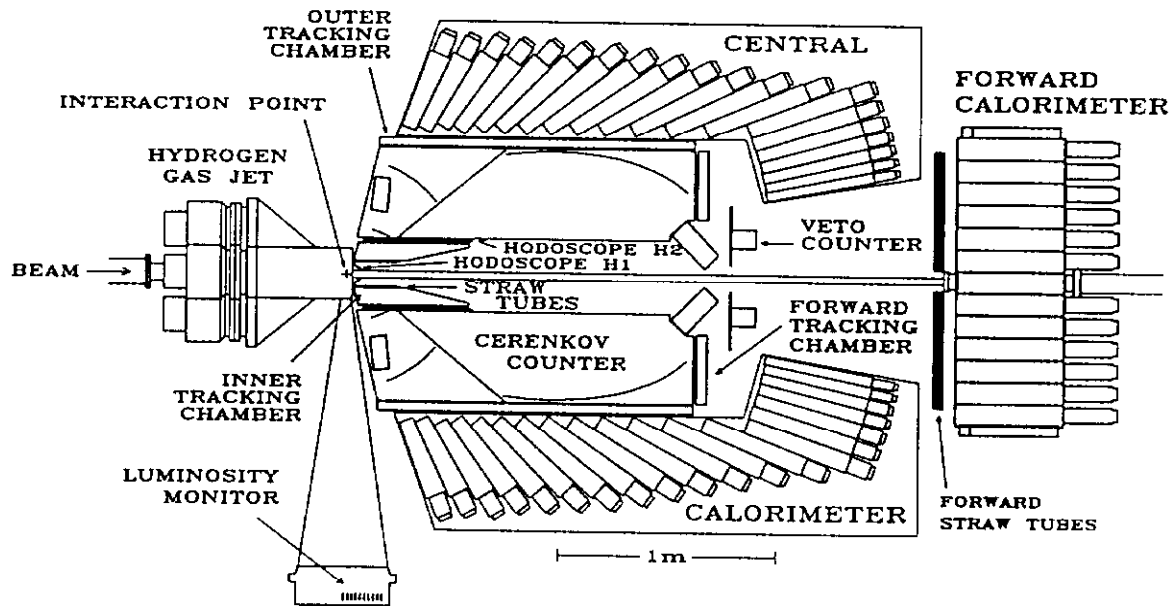


FIG. 2. E-760 equipment layout.

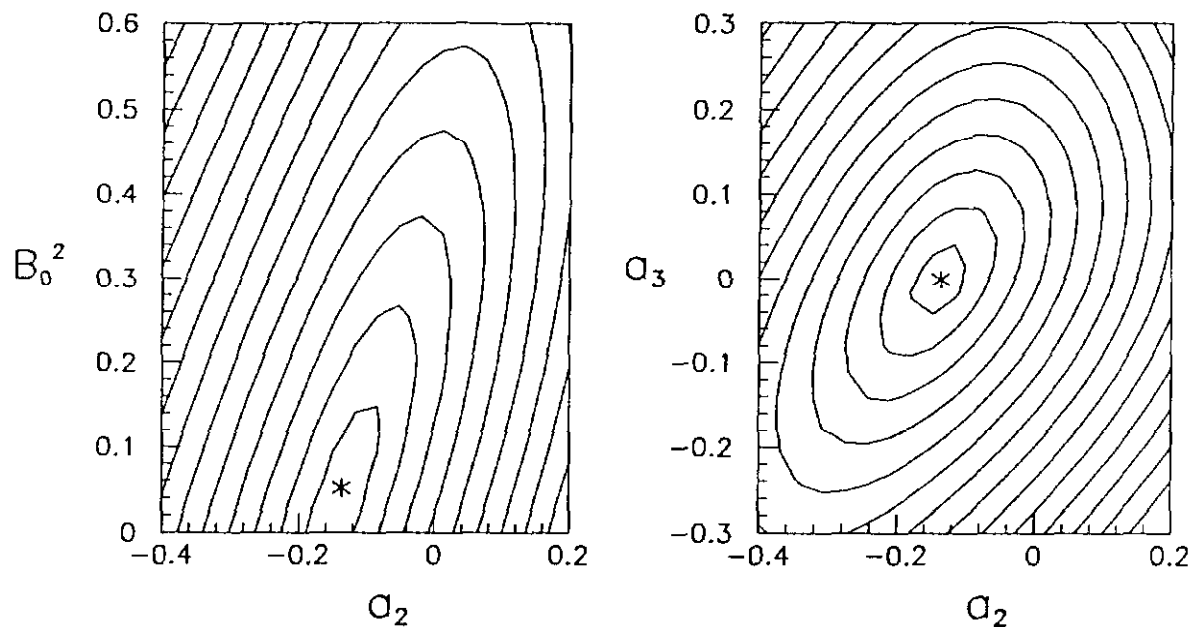


FIG. 3. Likelihood contours (a) in the a_2 - B_0^2 plane, with $a_3 = 0$, and (b) in the a_2 - a_3 plane, with $B_0^2 = 0.05$. The maximum is indicated by a star, and the contour lines correspond to 1,2,3... standard deviations.

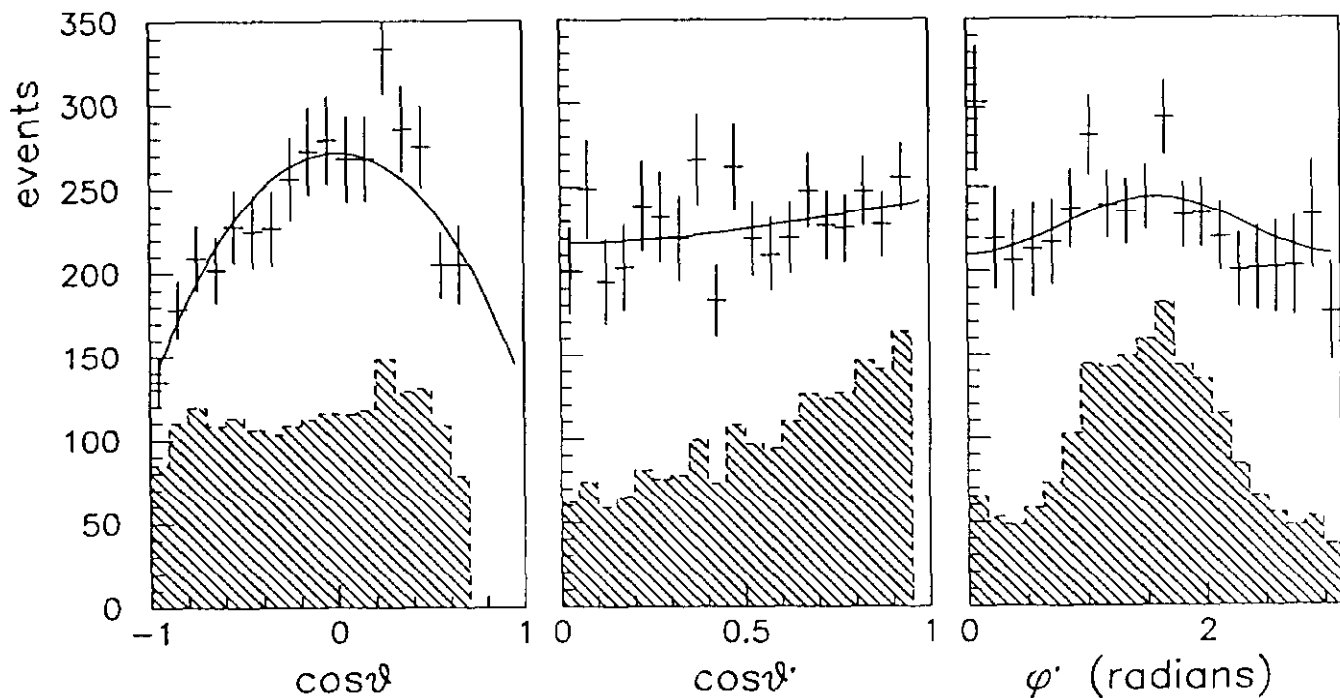


FIG. 4. Comparison of data (corrected for efficiency and acceptance) with the theoretical angular distribution function. The solid line shows the function $W(\theta, \theta', \phi')$ with $a_2 = -0.14$ and $B_0^2 = 0.05$; the shaded histograms show uncorrected data.

TABLES

TABLE I. Results of the likelihood fits.

	a_2	a_3	B_0^2
fit 1	$-0.14^{+0.06}_{-0.06}$	0.00 (fixed)	$0.05^{+0.11}_{-0.12}$
fit 2	$-0.14^{+0.08}_{-0.07}$	$0.00^{+0.06}_{-0.05}$	$0.05^{+0.14}_{-0.13}$

TABLE II. Coefficients K_i and functions T_i of Eq. (A1).

i	$T_i(\theta, \theta', \phi')$	$K_i(R, A_0, A_1, A_2)$
1	1	$\frac{1}{8}(2A_0^2 + 3A_2^2 - R(2A_0^2 - 4A_1^2 + A_2^2))$
2	$\cos^2 \theta$	$\frac{3}{4}(-2A_0^2 + 4A_1^2 - A_2^2 + R(4A_0^2 - 6A_1^2 + A_2^2))$
3	$\cos^4 \theta$	$\frac{1}{8}(6A_0^2 - 8A_1^2 + A_2^2)(3 - 5R)$
4	$\cos^2 \theta'$	$\frac{1}{8}(2A_0^2 + 3A_2^2 - R(2A_0^2 + 4A_1^2 + A_2^2))$
5	$\cos^2 \theta' \cos^2 \theta$	$\frac{3}{4}(-2A_0^2 - 4A_1^2 - A_2^2 + R(4A_0^2 + 6A_1^2 + A_2^2))$
6	$\cos^2 \theta' \cos^4 \theta$	$\frac{1}{8}(6A_0^2 + 8A_1^2 + A_2^2)(3 - 5R)$
7	$\sin^2 \theta' \cos 2\phi'$	$\frac{\sqrt{6}}{4}(R - 1)A_0A_2$
8	$\cos^2 \theta \sin^2 \theta' \cos 2\phi'$	$\frac{\sqrt{6}}{4}(4 - 6R)A_0A_2$
9	$\cos^4 \theta \sin^2 \theta' \cos 2\phi'$	$\frac{\sqrt{6}}{4}(5R - 3)A_0A_2$
10	$\sin 2\theta \sin 2\theta' \cos \phi'$	$-\frac{\sqrt{3}}{4}(A_0A_1 + \sqrt{\frac{3}{2}}A_1A_2 - R(2A_0A_1 + \sqrt{\frac{3}{2}}A_1A_2))$
11	$\cos^2 \theta \sin 2\theta \sin 2\theta' \cos \phi'$	$-\frac{1}{4\sqrt{3}}(5R - 3)(3A_0A_1 + \sqrt{\frac{3}{2}}A_1A_2)$